RSC Advances

PAPER

View Article Online
View Journal | View Issue

Cite this: *RSC Adv.*, 2022, **12**, 1341

Selective catalytic reduction of NO_x by low-temperature NH_3 over Mn_xZr_1 mixed-oxide catalysts

Shuaibo Zhang, Haixia Li, * Anchao Zhang, * Zhijun Sun, Xinmin Zhang, Changze Yang, Leying Jin and Zhiheng Song

Received 3rd December 2021
Accepted 21st December 2021

DOI: 10.1039/d1ra08800a

rsc.li/rsc-advances

Mn_xZr_1 series catalysts were prepared by a coprecipitation method. The effect of zirconium doping on the NH_3-SCR performance of the MnO_x catalyst was studied, and the influence of the calcination temperature on the catalyst activity was explored. The results showed that the Mn_6Zr_1 catalyst exhibited good NH_3-SCR activity when calcined at 400 °C. When the reaction temperature was 125–250 °C, the NO_x conversion rate of Mn_6Zr_1 catalyst reached more than 90%, and the optimal conversion efficiency reached 97%. In addition, the Mn_6Zr_1 catalyst showed excellent SO_2 and H_2O resistance at the optimum reaction temperature. Meanwhile, the catalysts were characterized. The results showed that the morphology of the MnO_x catalyst was significantly changed, whereby as the proportion of Mn^{4+} and O_α species increased, the physical properties of the catalyst were improved. In addition, both Lewis acid sites and Brønsted acid sites existed in the Mn_6Zr_1 catalyst, which reduced the reduction temperature of the catalyst. In summary, zirconium doping successfully improved the NH_3-SCR performance of MnO_x.

1. Introduction

With the exploitation of fossil fuels, severe pollution has been caused to the atmosphere, with nitrogen oxide (NO_x) being one of the most important pollutants. Therefore, NO_x removal is critical. At present, the most effective way to remove NO_x is through NH_3 selective catalytic reduction (NH_3-SCR).[1,2] However, the commercial V_2O_5/TiO_2 catalysts used in this technique have excellent deoxidation activity only at high temperatures and have a narrow operating temperature window (350–450 °C). The activity of the V_2O_5/TiO_2 catalyst is poor at low temperatures and can cause V poisoning and other shortcomings.[3,4] In addition, the presence of abundant SO_2 gas in the flue gas will cause deactivation of the V_2O_5/TiO_2 catalyst.[4,5] To solve this problem, SCR equipment should be installed downstream of the SO_2 removal unit. However, the downstream temperature is about 200 °C, which is unable to achieve the optimal reaction temperature of the V_2O_5/TiO_2 catalyst.[6] Therefore, the development of low-temperature, high-activity catalysts is significant.

The most widely studied catalysts are transition metal catalysts, rare earth metal catalysts, and zeolite catalysts. For transition metal catalysts, manganese oxide (MnO_x) has attracted much attention because of its excellent SCR performance. Jiang *et al.*[7] prepared the Mn-MOF-74 metal–organic framework by a hydrothermal method and formed spherical mesoporous manganese oxide nanoparticles by thermal decomposition. The catalyst has the characteristics of a large specific surface area and efficient denitration performance. However, when MnO_x meets water and sulfur, the MnO_x catalyst is easily deactivated, which seriously affects the denitrification activity. Casapu *et al.*[8] reported that SO_2 poisoning would lead to the irreversible redox capacity of the catalyst. Therefore, it is necessary to enhance the water resistance and sulfur resistance of MnO_x. Gao *et al.*[9] added Co to MnO_x by a complexation esterification, and the catalyst showed excellent activity and an enhanced corrosion resistance of MnO_x to SO_2. Wang *et al.*[10] showed that the Fe–Mn/Al_2O_3 catalyst at 150 °C had a NO conversion rate of more than 99%, N_2 selectivity of more than 98%, and strong SO_2 and H_2O corrosion resistance. Thus, the addition of one or more transition metals to MnO_x can make the catalyst have better sulfur resistance and water resistance.

Zirconium has received much attention due to its excellent thermal stability and surface acidity. Gao *et al.*[11] prepared a superacid catalyst by loading cerium oxide on zirconia sulfate, which significantly improved the SCR performance of the catalyst. The zirconium additive can increase the dispersion and activity of the catalyst, and enhance the sulfur resistance of the catalyst.[12] Shi *et al.*[5] improved the high-temperature activity and N_2 selectivity of the catalysts by introducing zirconium into V_2O_5/WO_3–TiO_2.

Therefore, zirconium was doped in MnO_x catalyst in this study to prepare a highly efficient SCR catalyst. In addition, the calcination temperature has a significant effect on the activity of the catalyst. Chen *et al.*[13] found that different calcination temperatures have many effects on $MnAlO_x$ catalysts, with the

School of Mechanical and Power Engineering, Henan Polytechnic University, Jiaozuo 454000, China. E-mail: lihx@hpu.edu.cn

most excellent activity at 400 °C, while the activity of the catalysts calcined at 600 °C decreased sharply. Fang *et al.*[14] also found that the calcination of Fe–Mn–Zr catalysts at different calcination temperatures not only affected the activity of the catalyst, but also changed the surface structure of the catalyst. Furthermore, when the calcination temperature was 800 °C, the catalyst had very poor tolerance to SO_2, and the NO conversion efficiency was only 20%. Therefore, study of the calcination temperature is critical.

In the present study, a series of new Mn_xZr_1 catalysts was prepared by a coprecipitation method, and the effects of the Mn/Zr ratio and calcination temperature on the activity and SO_2 and H_2O resistance of the catalysts were studied. In addition, the denitration activity was tested in a simulated gas in a fixed-bed reactor. Moreover, the physicochemical properties of the catalysts were studied by a temperature-programmed technique, SEM, FTIR, XRD, BET, XPS, H_2-TPR, NH_3-TPD, and other related experiments and characterization.

2. Experimental

2.1 Materials and reagents

$Mn(NO_3)_2 \cdot 4H_2O$ (≥99.0%, MACKLIN, Shanghai), $Zr(NO_3)_4 \cdot 5H_2O$ (≥99.0%, MACKLIN, Shanghai) and related metal nitrates were used as the precursor for the catalyst preparation. NaOH (≥96.0%, MACKLIN, Shanghai) was used to regulate the pH, while $(NH_4)_2CO_3$ (≥40.0%, Hongyan, Tianjin) was used as the precipitator. In this study, none of the reagents used needed to be further purified.

2.2 Catalyst preparation

A series of Mn_xZr_1 catalysts was prepared by a coprecipitation method. Taking the Mn_6Zr_1 catalyst as an example, the preparation method of the catalyst is described in detail. Specifically, a certain amount of $Mn(NO_3)_2 \cdot 4H_2O$ and $Zr(NO_3)_4 \cdot 5H_2O$ were added to a 300 mL beaker at room temperature, and then 100 mL distilled water was added, and for the sample where Mn : Zr = 6 : 1 (molar ratio), the prepared catalyst was named Mn_6Zr_1 according to the molar ratio of elements. The solution beaker was then put into a constant temperature magnetic stirring pot for rapid stirring and dissolution. After 30 min, a certain amount of 0.5 mol L^{-1} $(NH_4)_2CO_3$ solution was gradually added, and then 0.5 mol L^{-1} NaOH solution was gradually dropped in to make pH 9, and the solution was stirred for another 2 h. Then, the solution was aged at room temperature for 24 h, and afterward the supernatant was poured out, the sediment in the cup was collected, and the sediment was washed to neutral with deionized water. The cleaned samples were dried in a vacuum drying oven at 105 °C, and the calcination temperature was set at 400 °C in a muffle furnace, and the calcination temperature was set at the set temperature for 3 h (the heating rate was 5 °C min^{-1}). Ultimately, a solid was obtained and collected and sieved using a 40–60 mesh to the obtain Mn_6Zr_1 catalyst.

Mn_2Zr_1, Mn_4Zr_1, and Mn_8Zr_1 were prepared in the same way as Mn_6Zr_1, except that the molar ratio of elements was different when the material precursor was added. The preparation methods for Mn_6Zr_1-300 °C, Mn_6Zr_1-500 °C, Mn_6Zr_1-600 °C, and Mn_6Zr_1-700 °C were the same as for Mn_6Zr_1, but the final calcination temperature was changed.

2.3 Catalytic performance test

The activity of the catalyst was evaluated and detected by using temperature-programmed technology, as shown in Fig. 1. Each test catalyst (0.2 g, 40–60 mesh) was placed in a fixed-bed quartz reactor (diameter = 9 mm, length = 60 cm) for the NH_3-SCR activity evaluation test. The reaction conditions for traditional NH_3-SCR denitration are as follows: 500 ppm NO, 500 ppm NH_3, 5 vol% O_2, 100–200 ppm SO_2 (when used), 5 vol% H_2O (when used), and N_2 as the balance gas. The total flow rate of the gas was 500 mL min^{-1} controlled by mass flow controllers (Beijing Sevenstar Flow Co., Ltd, China). The gas hourly space velocity was set as 30 000 h^{-1}. The reaction temperature was 100–300 °C when the catalyst activity was tested. The concentration of NO_x and NH_3 before and after the reaction was directly measured online by a flue gas analyzer. The remaining unconverted gas was filtered by NaOH solution. Each temperature point was kept for 30 min, and the data were recorded in a stable numerical state. The NO_x conversion rate formula is as follows:

$$NO_x \text{ conversion} = \frac{[NO_x]_{in} - [NO_x]_{out}}{[NO_x]_{in}} \times 100\% \quad (1)$$

$$N_2 \text{ selectivity } (\%) = \left(1 - \frac{2[N_2O]_{out} + [NO_2]_{out} - 2[N_2O]_{in} - [NO_2]_{in}}{[NH_3]_{in} + [NO_x]_{in} - [NH_3]_{out} - [NO_x]_{out}}\right) \times 100\% \quad (2)$$

The reaction rate of NH_3-SCR can be truly reflected by the turnover frequency (TOF), and the calculation formula for this is as follows:[15,16]

$$TOF = \frac{v \times \alpha}{V_m \times n_a} \quad (3)$$

where v represents the flow rate of NO (m^3 s^{-1}), α is the NO conversion at a specific temperature (%), V_m is the gas molar constant (m^3 mol^{-1}), and n_a is the mole number of surface acid sites molar amount (mol), which was estimated based on NH_3-TPD.

The SCR activity of the catalyst can also be quantitatively expressed by a first-order rate constant (k), which can be calculated by the formula for NO conversion (x) as follows:[16,17]

$$k = -\frac{F_0}{[NO]_0 W} \ln(1 - x) \quad (4)$$

$$\ln k = -\frac{E_a}{RT} + \ln A \quad (5)$$

where F_0 is the NO feeding rate, $[NO]_0$ is the NO concentration at the inlet, W is the catalyst dosage, E_a is the apparent activation

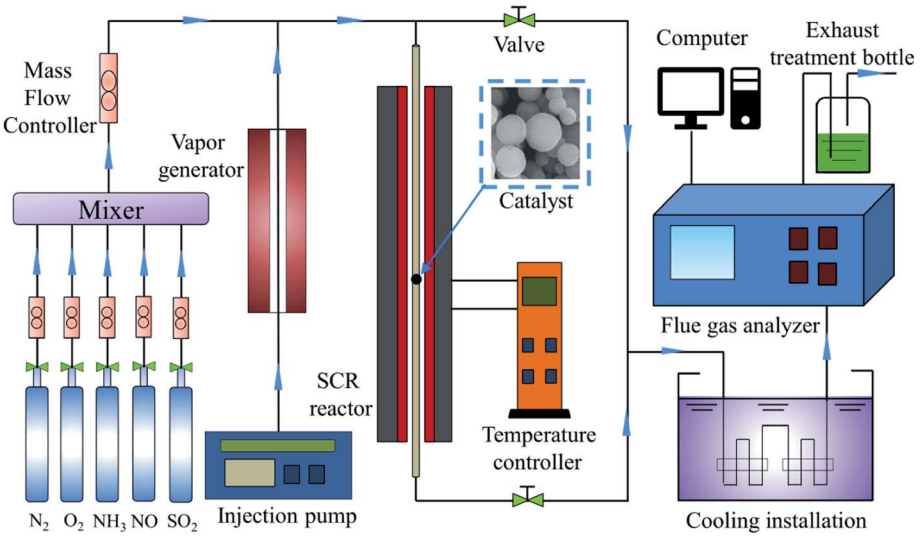

Fig. 1 Catalytic activity evaluation device.

energy, T is the Kelvin temperature, R is the gas constant, and A is the pre-factor.

2.4 Catalyst characterization

Fourier transform infrared spectroscopy (FTIR) was used to determine the species on the catalyst surface in the range of 400–4000 cm^{-1} by infrared spectrometry (Nicolet iS5). Scanning electron microscope (SEM; Hitachi Company Japan) was used to analyze the morphology of the catalysts. Before the test, the sample was evenly smeared on the surface of the conductive adhesive, and then sprayed with gold. The N_2 adsorption–desorption isotherms of the catalysts were determined on a Quantachrome Instrument (Quadrasorb EVO) with high-purity N_2 as the adsorbent. Before each analysis, the catalysts were degassed in a vacuum at 300 °C for 3 h and the isotherms were measured in a liquid nitrogen N_2 state (−196 °C). The X-ray diffraction (XRD) test was carried out with Cu Kα radiation (λ = 0.15418 nm) at 40 kV and 40 mA in an X-ray tube by using a Brook D8 Advance system (Germany). The scanning range was 10–80°. The speed was 6° min^{-1}. The XPS tester used the Escalab 250XI spectrometer (Semer, Inc), operating under monochrome Al Kα radiation (1486.6 eV), 12 kV, and 15 mA ultra-high vacuum, and all the binding energies were calibrated by the C 1s peak at 284.4 eV. Temperature-programmed reduction of H_2 (H_2-TPR) and temperature-programmed desorption of NH_3 (NH_3-TPD) were performed on a Mac AutoChem II 2920 instrument (USA). The former was pretreated in 300 °C argon at a flow rate of 20 mL min^{-1} for 1 h and cooled to room temperature. The gas was converted into a mixture of 5 vol% H_2–N_2 at a flow rate of 30 mL min^{-1}. After a straight baseline, the catalyst was heated from room temperature to 800 °C at a rate of 10 °C min^{-1}. The latter was pretreated in 300 °C argon at a flow rate of 20 mL min^{-1} for 1 h and then cooled to room temperature. The samples were then exposed to a mixture of 5 vol% NH_3–N_2 for 1 h, and then purified with high-purity He at a flow rate of 20 mL min^{-1} to remove the physically adsorbed NH_3. After the baseline was stabilized, the sample was heated from room temperature to 800 °C at a rate of 10 °C min^{-1}.

3 Results and discussion

3.1 Catalytic activity of Mn_xZr_1 catalysts

The NO_x conversion efficiency of the Mn_xZr_1 series catalyst is shown in Fig. 2a and Table 1. It could be found that with the increase in the manganese element ratio, the catalyst activity increased first and then decreased. First, the Mn_6Zr_1 catalyst showed the best activity. The conversion efficiency reached more than 90% at 125–250 °C, while the highest conversion efficiency reached 97%. It had a good temperature window and excellent activity. Second, it is worth noting that the Mn_8Zr_1 catalyst showed the best activity at 100 °C, with the conversion efficiency reaching 95%, although the overall conversion efficiency decreased. A reasonable explanation for this is that while an appropriate ratio of manganese to zirconium can significantly improve the activity of the MnO_x catalyst, too much manganese will mask the active sites on the surface of the catalyst, thus reducing the activity of the catalyst.

The N_2 selectivity of the Mn_xZr_1 series catalyst is shown in Fig. 2b. The N_2 selectivity of the catalysts decreased with increasing temperature. The main reason for this is that the by-products NO_x and N_2O were produced by NH_3 oxidation.[18] Mn_2Zr_1 had the lowest N_2 selectivity and Mn_6Zr_1 had the best N_2 selectivity. Such results are similar to the NO_x conversion efficiency, and also indicated that Mn_6Zr_1 has a strong redox performance.[19] The selectivity of N_2 in MnO_x was second only to Mn_6Zr_1, but the conversion efficiency of NO_x was the lowest, which may be due to the weak redox capacity of MnO_x, which produced less N_2O.[20]

As is well known, the calcination temperature of a catalyst directly affects its SCR activity. Fig. 2c shows the NO_x conversion of the Mn_6Zr_1 catalyst at different calcination temperatures

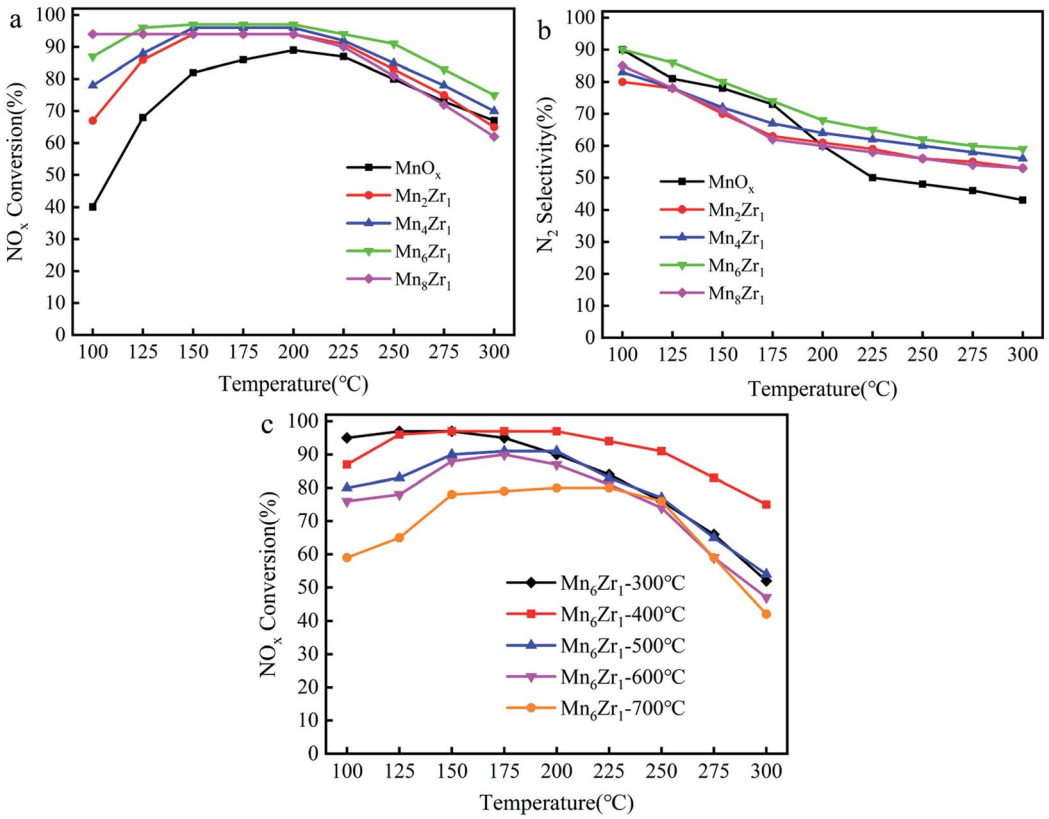

Fig. 2 (a) NO_x conversion at different ratios of Mn/Zr, (b) N_2 selectivity at different ratios of Mn/Zr, and (c) conversion rate of Mn_6Zr_1 at different calcination temperatures.

Table 1 Catalytic performance of MnO_x and Mn_xZr_1 catalysts

Temperature (°C)	NO_x conversion (%)				
	MnO_x	Mn_2Zr_1	Mn_4Zr_1	Mn_6Zr_1	Mn_8Zr_1
100	40	67	78	87	94
125	68	86	88	96	94
150	82	94	96	97	94
175	86	94	96	97	94
200	89	94	96	97	94
225	87	91	92	94	90
250	80	83	85	91	81
275	73	75	78	83	72
300	67	65	70	75	62

(300–700 °C). The Mn_6Zr_1-300 °C catalyst only showed the best activity at 100–150 °C, which may be because of the calcination temperature and not being able to expose more active sites. When the calcination temperature was 400–700 °C, the NO_x conversion decreased gradually. In conclusion, the Mn_6Zr_1 catalyst showed the best catalytic activity when the calcination temperature was 400 °C.

The tolerance of the Mn_6Zr_1 catalyst to SO_2 and H_2O in a flue gas atmosphere was simulated at 200 °C. The tolerance test results for 100 ppm and 200 ppm SO_2 on the catalyst are shown in Fig. 3. When 100 ppm SO_2 was introduced, the catalyst conversion rate gradually decreased, and finally stabilizes at 90% after 4 h. When introducing 200 ppm SO_2, the NO_x conversion rate of Mn_6Zr_1 decreased from 90% at 100 ppm to 82% at 200 ppm. This may be due to the formation of sulfate on the catalyst's surface by SO_2, thus covering its active site. When SO_2 was turned off, the NO_x conversion rate recovered to 95%, indicating that the catalyst was reversible. However, the Mn_6Zr_1 catalyst did not fully recover to its previous levels, probably because the sulfate formed by the reaction of SO_2 with NH_3 or metal oxides was challenging to decompose at low temperatures, thus blocking some of the active or acidic sites of the catalyst, leading to a decrease in catalytic activity.[21] When 5% H_2O was added, the catalyst conversion efficiency of the catalyst decreased and stabilized at 92% after 8 h. Compared with the optimal conversion efficiency of 97%, it decreased by 5%. When the water vapor was turned off, the NO_x conversion rate recovered to 96%, indicating that the catalyst was reversible, basically going back to the original conversion efficiency. In summary, the Mn_6Zr_1 catalyst showed good resistance to sulfur and water.

As can be seen from Fig. 8 and Fig. 3 that Mn_6Zr_1 had good NO_x removal ability, and excellent sulfur resistance and water resistance. Therefore, the anti-SO_2 and anti-H_2O properties of the Mn_6Zr_1 catalyst were further tested. As shown in Fig. 4, when 100 ppm SO_2 (stage I) was introduced into the Mn_6Zr_1 catalyst, the conversion efficiency reached 92%. Further additions of 5% H_2O (stage II) reduced the conversion efficiency to

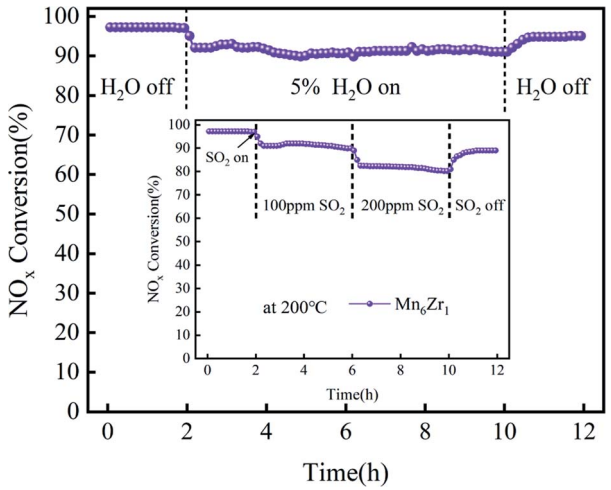

Fig. 3 Resistance of the Mn_6Zr_1 catalyst to H_2O and SO_2 at 200 °C.

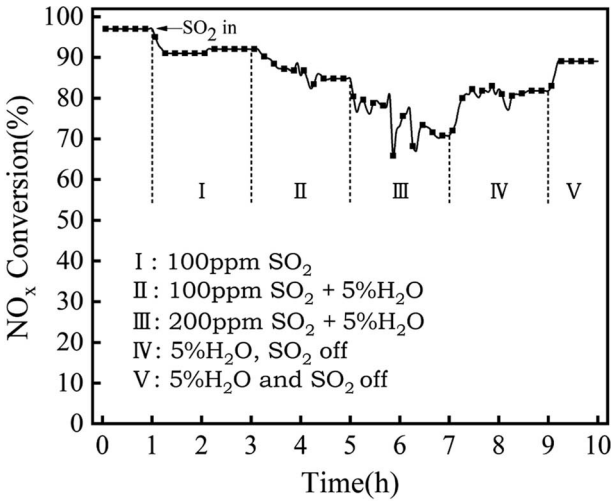

Fig. 4 NH_3-SCR activity of Mn_6Zr_1-400 °C in the presence of SO_2 and H_2O at 200 °C.

85%, indicating that H_2O inhibited the adsorption activity of NH_3. When 200 ppm SO_2 and 5% H_2O (stage III) were introduced, the conversion efficiency of NO_x reached 71% after 2 h of stability, which may be due to the formation of $(NH_3)_2SO_4$ and $(NH_3)_2SO_3$ by-products on the catalyst's surface, resulting in a decrease in catalytic activity.[14] When SO_2 was turned off (stage IV), the conversion efficiency increased gradually and then remained at 82%. This may be because the H_2O washed away the by-products on the catalyst's surface, releasing some of the active sites. The NO_x conversion efficiency reached about 90% when H_2O was turned off (stage V). These results show that the adsorption of SO_2, H_2O, and reaction gas on the surface is competitive and the deactivation is reversible.

3.2 Characterization of the Mn_xZr_1 catalysts

3.2.1 XRD. The Mn_xZr_1 series catalysts, MnO_x, and ZrO_2 were characterized by XRD, as shown in Fig. 5a. The diffraction peaks of ZrO_2 were not consistent with those of Mn/Zr catalysts with different proportions, indicating that ZrO_2 formed an amorphous structure or was well dispersed on the catalyst surface. The diffraction peak of pure MnO_x showed the presence of MnO_2 (PDF#12-0141) and Mn_3O_4 (PDF#04-0732). When the Mn/Zr ratio increased, the diffraction peak of MnO_x in the Mn_xZr_1 series of catalysts decreased or disappeared gradually, indicating that MnO_x was highly dispersed on the catalyst's surface, especially as the diffraction peak of the Mn_6Zr_1 catalyst was the weakest. In addition, the amorphous structure is conducive to enhancing the activity of the catalyst,[22] which also well proved the good catalytic activity of Mn_6Zr_1.

Fig. 5b shows the diffraction spectrum of the Mn_6Zr_1 catalyst at 300–700 °C. When the calcination temperature of the catalyst increased, the diffraction peak of the catalyst became more apparent, and the diffraction peak of ZrO_2 (PDF#50-1089) appeared. The crystal structure of the catalyst will be formed at a higher calcination temperature, which will inhibit the activity of the catalyst. This is also why the catalyst activity was poor when the calcination temperature was 500 °C or above. When the calcination temperature was 300 °C and 400 °C, the crystallinity of the Mn_6Zr_1 catalyst was poor, which is conducive to enhancing the activity of the catalyst. Besides, when the calcination temperature was 400 °C, the diffraction peak of the Mn_6Zr_1 catalyst was wide and weak in the 2θ range of 25–35°, and seemed to be a mixed oxide of Mn_2O_3 and Mn_3O_4.

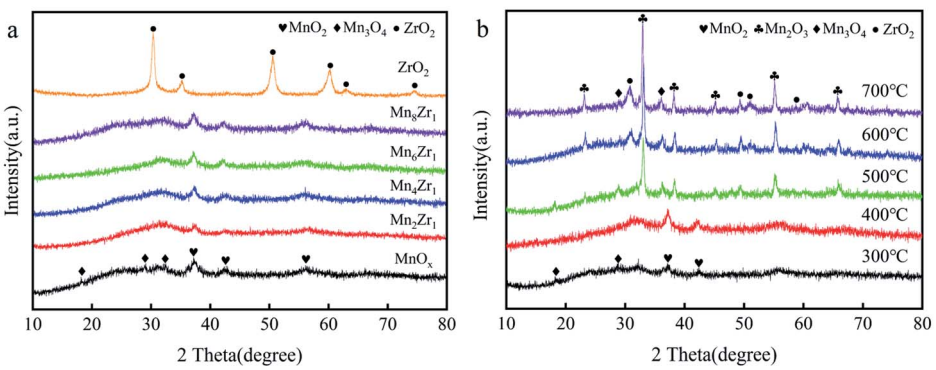

Fig. 5 (a) XRD patterns of Mn_xZr_1 catalysts and (b) XRD patterns of Mn_6Zr_1 catalysts calcined at different temperatures.

Moreover, the vast peak structure contributed to the adsorption/desorption of the catalyst surface and the redox reaction.[23]

3.2.2 FTIR. The FTIR spectra of the samples detected within the range of 450–4000 cm^{-1} are shown in Fig. 6. Two samples had a wide absorption band at 3421 cm^{-1}, attributed to stretching vibrations of hydroxide and hydroxyl groups in interlayer water molecules.[19] An angular deformation vibration of water molecules was observed in two samples at 1628 cm^{-1}.[24] The absorption band at 1385 cm^{-1} in the spectrum could be attributed to the stretching vibration of NO_3^-, indicating that there were NO_3^- ions in the interlayer of the catalyst to balance the charge of the hydroxyl base.[25] Meanwhile, a new weak adsorption band was observed near 1099 cm^{-1}, caused by the antisymmetric stretching vibration of the tetrahedral MnO_4^- interlayer $\nu 3$.[26] Finally, the vibrations in the range of 500–800 cm^{-1} were mainly M–O lattice vibrations (ν_{M-OH}, ν_{M-O-M}, or ν_{O-M-O}).[27] Through FTIR spectrum analysis of the sample precursor and the XRD analysis above, the successful synthesis of the catalyst was confirmed.

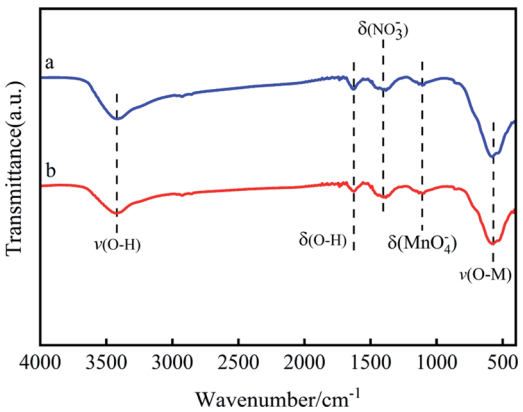

Fig. 6 FTIR spectra of (a) MnO_x, (b) Mn_6Zr_1.

3.2.3 SEM. Fig. 7 shows the surface morphologies of the MnO_x, ZrO_x, and Mn_6Zr_1 catalysts. As shown in Fig. 7a and b, MnO_x had an irregular spherical structure with an uneven surface. Fig. 7c shows the crystal morphology of ZrO_x, which had a block structure. As shown from Fig. 7d and e, the Mn_6Zr_1 catalyst became a uniform cube structure as a whole, and its surface became very smooth. It seems that MnO_x had been modified by zirconium. As can be seen from Fig. 7f, many white spots were formed on the surface of the Mn_6Zr_1 catalyst, indicating that the zirconium element was successfully attached to the surface of the catalyst. It was well dispersed on the catalyst surface, which is consistent with the XRD characterization of Mn_6Zr_1. Zirconium can increase the active sites of the catalyst.[28] Therefore, the reaction molecules can be captured better during the SCR denitration process, thus improving the activity of the catalyst.

3.2.4 BET. Fig. 8 shows the N_2 adsorption isotherms and pore-size distribution of the three catalysts at liquid nitrogen temperature. The corresponding physical properties are shown in Table 2. In Fig. 8a, the isotherms of the three catalysts are typical IV-type curves, and all of them have hysteresis loops. When P/P_0 was 0.4, the adsorption capacity of N_2 increased rapidly, indicating the presence of a microporous structure in the catalyst.[29]

Fig. 8b shows the pore-size distribution of the catalysts. The results showed a peak at about 2 nm for MnO_x and Mn_6Zr_1 catalysts, and a broad peak at 3–7 nm for all three catalysts, indicating that the samples were dominated by intermediate

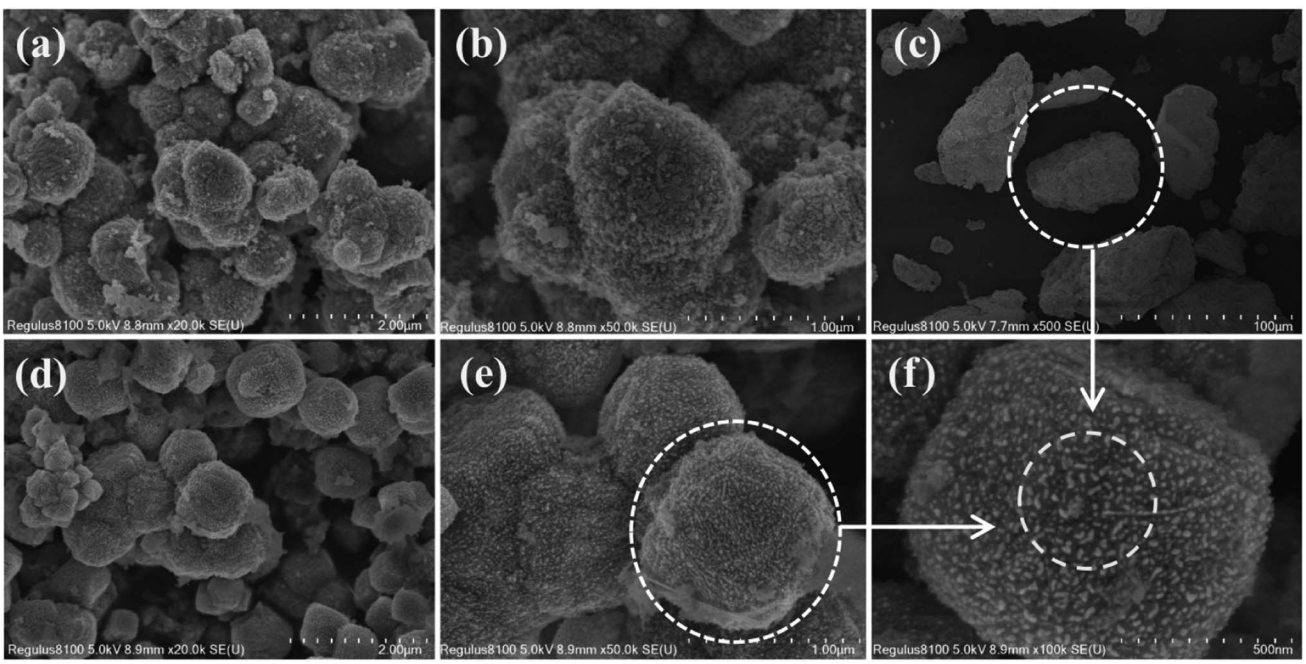

Fig. 7 SEM images of (a and b) MnO_x, (c) ZrO_2, and (d–f) Mn_6Zr_1.

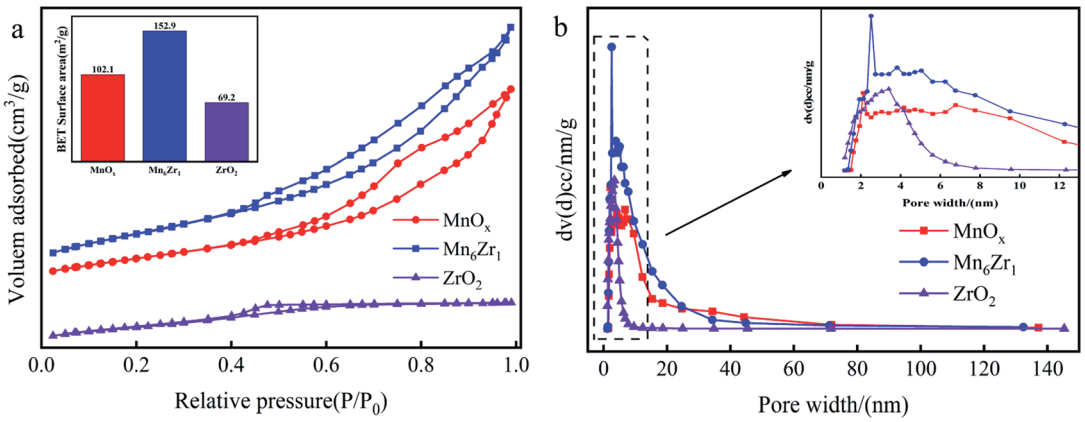

Fig. 8 N_2 adsorption isotherms (a) and pore-size distributions (b) of MnO_x, ZrO_2, and Mn_6Zr_1.

Table 2 BET surface areas, pore volume, and average pore diameter of the samples

Samples	Surface area ($m^2\ g^{-1}$)	Pore volume ($cm^3\ g^{-1}$)	Average pore diameter (nm)
MnO_x	102	0.22	2.1
ZrO_2	69	0.05	3.4
Mn_6Zr_1	153	0.28	2.5

pores and supplemented by micropores. There were many intermediate pores in the catalyst, which are conducive to NO_x removal and thus show good catalytic activity.[30] From Table 1, the specific surface area and pore volume of the manganese-based catalyst were significantly improved by adding zirconium. The specific surface area and pore volume of the Mn_6Zr_1 catalyst were increased to 153 $m^2\ g^{-1}$ and 0.28 $cm^3\ g^{-1}$, respectively. The higher specific surface area can better adsorb reactants, hence promoting the activity of the catalyst.

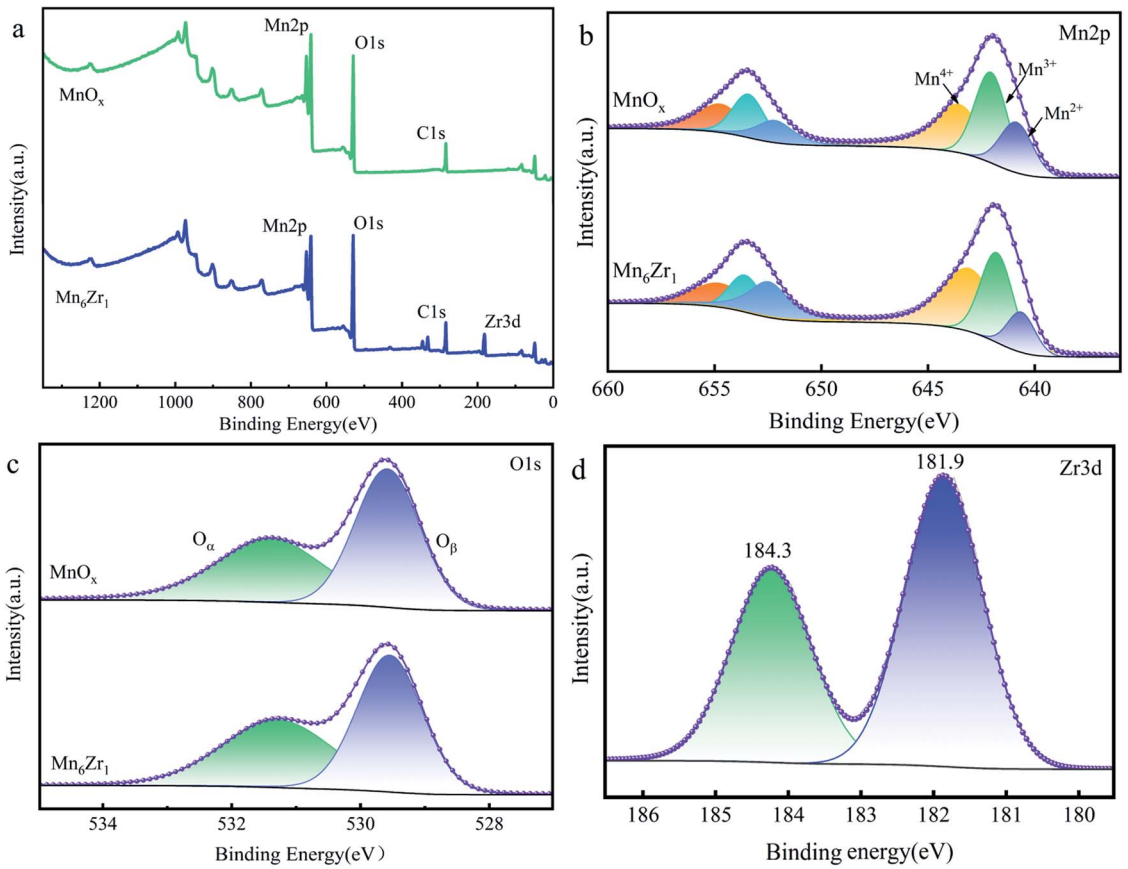

Fig. 9 XPS spectra of (a) the survey, (b) Mn 2p, (c) O 1s, and (d) Zr 3d of the MnO_x and Mn_6Zr_1.

Furthermore, the pore size of the Mn_6Zr_1 catalyst was increased to 2.5 nm, making it easier for the reaction gas to pass through the catalyst.

3.2.5 XPS. The surface elemental states of the MnO_x and Mn_6Zr_1 catalysts were detected using the XPS technique, and the results are shown in Fig. 9 and Table 3. The full spectrum of Fig. 9a confirmed the existence of Mn, Zr, C, and O elements. Fig. 9b shows the XPS spectra of Mn 2p. Through peak fitting deconvolution for the MnO_x catalyst, Mn $2p_{3/2}$ was divided into three characteristic peaks, namely 643.5, 642.1, and 640.9 eV, respectively, which were successively assigned as Mn^{4+}, Mn^{3+}, and Mn^{2+}.[30,31] The three characteristic peaks of Mn^{4+}, Mn^{3+}, and Mn^{2+} in Mn $2p_{3/2}$ on the Mn_6Zr_1 catalyst were 643.1, 641.7, and 640.6 eV, respectively. In addition, the binding energy of Mn_6Zr_1 was lower than that of the MnO_x catalyst. According to the literature, elements with a lower binding energy have higher activity.[32] Meanwhile, the Mn^{3+}/Mn ratio of MnO_x was 2.57% higher than that of Mn_6Zr_1. However, the Mn^{4+}/Mn ratio of Mn_6Zr_1 was 46.54%, which was significantly higher than that of MnO_x (42.41%), indicating that a large number of MnO_2 species were added on the surface of Mn_6Zr_1. The results show that the Mn/Zr ratio can affect the valence state of Mn species. According to the literature, the activity sequence of MnO_x in low-temperature NH_3-SCR is MnO_2 > Mn_5O_8 > Mn_2O_3 > Mn_3O_4 > MnO. Therefore, more Mn^{4+} can promote the NO_x conversion efficiency, thus improving the catalytic capacity.[33]

The spectrum of O 1s is shown in Fig. 9c. The two fitting peaks of O 1s were at 529.8 and 531.5 eV, respectively. The former was for lattice oxygen O_β; while the latter was denoted as adsorbed oxygen O_α.[34] Table 2 shows that the $O_\alpha/(O_\alpha + O_\beta)$ value of the Mn_6Zr_1 catalyst was 47.94%, which was significantly higher than that of the MnO_x catalyst. It is well known that O_α can promote the oxidation of NO to NO_2 due to its high mobility and better oxidation capacity, hence speeding up the reaction rate of NH_3-SCR.[35]

Fig. 9d presents the XPS spectrum of Zr_3d. The binding energy of the Mn_6Zr_1 catalyst at Zr $3d_{5/2}$ was 181.9 eV. However, the binding energy of Zr $3d_{5/2}$ for pure ZrO_2 was 182.1 eV 14. The binding energy here is higher than that of the catalyst Mn_6Zr_1, indicating an interaction between manganese and zirconium in the Mn_6Zr_1 catalyst. With the increase in the Zr–O coordination bond length, not only is the surface acidity of the catalyst changed, but also the adsorption property of the catalyst surface is affected 30.

3.2.6 Temperature programming testing. In order to better study the surface acidity of the catalyst, NH_3-TPD experiments were conducted on the catalyst, and the results are shown in Fig. 10a. NH_3 adsorbed at the Brønsted acid site is more easily released than at the Lewis acid.[36,37] Therefore, the desorption peak of the Brønsted acid site is in the low-temperature range, and that of the Lewis acid site is in the high-temperature range.[38] The desorption peak of Mn_6Zr_1 catalyst at 100–200 °C may be due to the physical adsorption of NH_3 on the weak acid site, and part of the NH_4^+ ions were absorbed by the Brønsted acid site.[39] The desorption peaks at 200–400 °C should belong to the chemisorption of NH_3 at weak acid sites.[40] The peak at 400–500 °C belongs to the desorption peak of a medium-strong acid. In contrast, the desorption peak above 700 °C was attributed to a strong acid, which can be attributed to NH_3 or NH_4^+ adsorption on the Lewis acid site. Lewis acid sites have good stability

Table 3 XPS test results and apparent activation energy (E_a) of the MnO_x and Mn_6Zr_1 catalysts

	Atomic concentration (%)				Atomic radio (%)				
Samples	C	Mn	O	Zr	Mn^{3+}/Mn	Mn^{4+}/Mn	$O_\alpha/(O_\alpha + O_\beta)$	E_a (kJ mol^{-1})	ln A
MnO_x	27.96	22.37	49.67	—	36.89	42.41	46.92	38.96	11.78
Mn_6Zr_1	29.95	18.07	49	2.98	34.32	46.54	47.94	19.59	6.92

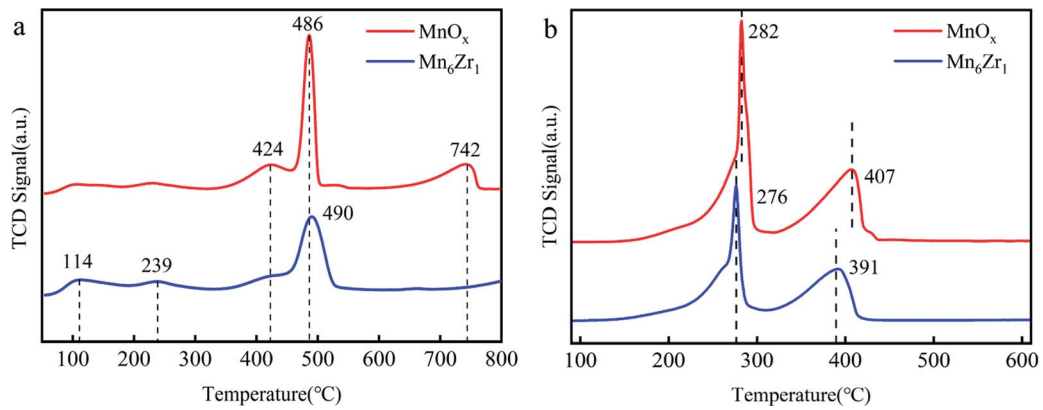

Fig. 10 NH_3-TPD (a) and H_2-TPR (b) of MnO_x and Mn_6Zr_1 catalysts.

and can work at a wide range of temperatures.[41] In addition, we found that the desorption peak of Mn_6Zr_1 catalyst was shifted toward the low-temperature region and contained Brønsted acid sites and Lewis acid sites. This indicated that the addition of zirconium changes the properties of MnO_x acid sites. In conclusion, the Mn_6Zr_1 catalyst has a wide window and good SCR activity at low-temperature.

H_2-TPR was used to evaluate the redox performance of each catalyst, as shown in Fig. 10b. Both MnO_x and Mn_6Zr_1 catalysts displayed two reduction peaks. The reduction process of manganese-based catalysts usually follows three steps: $Mn^{4+} \rightarrow Mn^{3+} \rightarrow Mn^{8/3+} \rightarrow Mn^{2+}$.[42,43] At 270–300 °C and 390–410 °C, both catalysts showed reduction peaks, attributed to the reduction of MnO_2 to Mn_2O_3 and Mn_2O_3 to Mn_3O_4,[42,44] respectively. It was found that the addition of zirconium reduced the reduction peak of the Mn_6Zr_1 catalyst. This indicated that the Mn_6Zr_1 catalyst had more vital redox capacity.[45] This also explains the reason why the Mn_6Zr_1 catalyst had an excellent low-temperature denitration activity.

3.3 NH_3-SCR kinetic studies

The turnover frequency (TOF) and the Arrhenius plots of the MnO_x and Mn_6Zr_1 catalysts are shown in Fig. 11. As can be seen, the TOF value of the Mn_6Zr_1 catalyst was much larger than that of the MnO_x catalyst at various temperature points, especially at 100–120 °C. The TOF value of the Mn_6Zr_1 catalyst was 2–3 times that of MnO_x. This result intuitively shows that the Mn_6Zr_1 catalyst has excellent SCR performance, and is consistent with the excellent N_2 selectivity. In addition, it can be seen from the Arrhenius figure that the MnO_x catalyst had a high activation energy (38.96 kJ mol^{-1}). The activation energy (19.59 kJ mol^{-1}) of the Mn_6Zr_1 catalyst decreased significantly when zirconium was doped in the catalyst, which increased the reaction rate of the catalyst. According to the existing literature, the lower the activation energy of a catalyst, the higher the catalytic SCR activity.[46]

3.4 Discussion

The catalyst structure, surface acid–base properties, oxygen mobility, and the interactions between the active components all affect the activity of a catalyst. Zirconium doping into the MnO_x catalyst can improve the activity of the catalyst, as well as the sulfur resistance and water resistance of the catalyst. In addition, the molar ratio of Mn/Zr also has a great influence on the catalyst. An excessive mole ratio may lead to surface blockage of the catalyst, while too small a molar ratio may lead to too few active sites, which will directly affect the activity of the catalyst. The calcination temperature also has a significant influence on the activity of the Mn_6Zr_1 catalyst: too high a calcination temperature tends to shrink the pore size and affect the gas entering the catalyst, thus inhibiting the absorption of the catalyst's active site.[14] Therefore, the catalyst cannot perform SCR reaction better. The Mn_6Zr_1 catalyst exhibited a sizable specific surface area, pore volume, and pore size at 400 °C. These factors all affect the conversion efficiency of the catalyst. The larger specific surface area will increase the adsorption sites on the catalyst surface, such as Brønsted and Lewis acid sites. The wider aperture provides convenience for gas diffusion, abundant mesopores can provide the main channel for gas to enter the catalyst, and improve the contact between gas and the inner surface, and thus promote the denitrification activity of the catalyst. From the crystal image, the diffraction peak of the Mn_6Zr_1 catalyst was weak, indicating that MnO_x and ZrO_2 formed an amorphous structure or were well dispersed on the catalyst surface. This is also one of the essential reasons for the excellent denitration performance of the Mn_6Zr_1 catalyst. The interaction between ZrO_2 and the active carrier will accelerate the oxidation rate of the catalyst and make the high-valence Mn easier to be reduced.[30] This is also a reasonable explanation for why catalyst reduction shifts to the low-temperature region.

The addition of zirconium increased the proportion of Mn^{4+} and decreased the proportion of Mn^{3+} in the Mn_6Zr_1 catalyst. The former mainly adsorbs NH_3, while the latter tends to adsorb NO.[47] When the sulfur resistance of the catalyst is measured at the optimal temperature, SO_2 will be oxidized by MnO_x to form

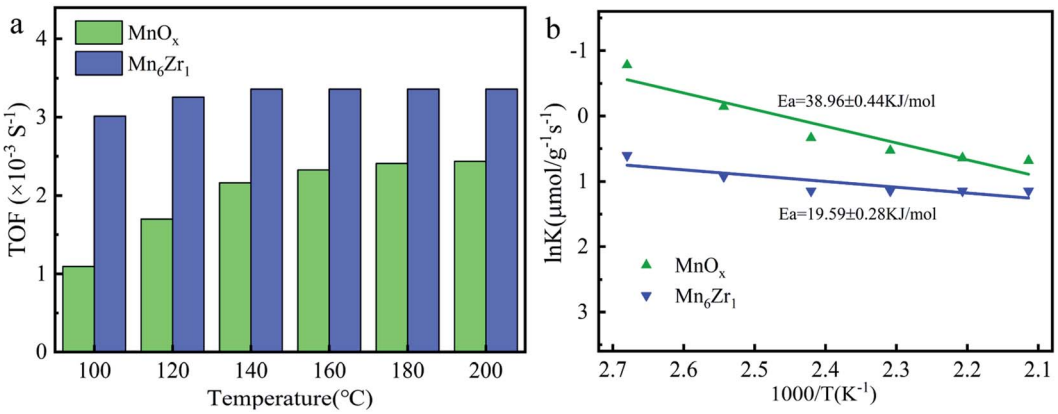

Fig. 11 (a) TOF and (b) Arrhenius plots of MnO_x and Mn_6Zr_1 catalysts at different temperatures.

sulfate, and Mn^{4+} will lose oxygen and convert to Mn^{3+}.[21] At this point, the relative content of Mn^{4+} will gradually decrease, and the adsorption of NH_3 will also gradually decrease. This will inhibit the formation of NH_4NO_3 and hinder the cyclic reaction of low-temperature SCR. On the contrary, the unadsorbed NH_3 will react with SO_2 to form $(NH_4)_2SO_4$, and the sulfate will precipitate on the surface of the catalyst, blocking the pores of the catalyst or covering the active sites on the catalyst surface, resulting in a decrease in the activity of the catalyst. More Mn^{4+} species will adsorb large amounts of NH_3, which will inhibit sulfate formation. This also explains the excellent sulfur resistance of the Mn_6Zr_1 catalyst with a high proportion of Mn^{4+} species. In addition, the surface of the Mn_6Zr_1 catalyst contained a large amount of adsorbed oxygen O_α. The adsorbed oxygen O_α has better mobility and activity in the NH3-SCR denitration reaction.

Mn^{4+}, Mn^{3+}, and Mn^{2+} species exist simultaneously in the Mn_6Zr_1 catalyst. Lattice oxygen O_β is first used in the process of NO removal by NH_3-SCR. At this time, Mn^{4+} species in the Mn_6Zr_1 catalyst will lose oxygen and generate low-price Mn^{3+} and Mn^{2+}. The Mn^{2+} species, on the other hand, tend to adsorb oxygen and convert it to lattice oxygen, thus forming an oxygen cycle: $O_2(g) \leftrightarrow O_2(a) \leftrightarrow O_2^-(a) \leftrightarrow 2O^-(a) \leftrightarrow 2O^{2-}$(lattice). The oxidation of NO is further promoted by the reversible adsorption/desorption cycle of lattice oxygen. Furthermore, the elimination of NO consists of two steps: (1) $NO + O_2 = N_xO_y$, (2) $N_xO_y + NH_3 = N_2 + H_2O$. NO is mainly bound to active oxides, including adsorbed oxygen O_α and lattice oxygen O_β. The intermediate N_xO_y is cleaved to the N–H bond in adsorbed NH_3, and H or NH_3 is bound to the hydroxyl group on the surface to form NH_4^+. The number of acid centers on the catalyst surface and the types of Lewis and Brønsted acid centers also affect the adsorption of NH_3. The zirconium-doped MnO_x catalyst has an increased Brønsted acid level on its surface, thus enhancing the adsorption capacity for NH_3 and promoting the activity of low-temperature SCR. For the Mn_6Zr_1 catalyst, amorphous ZrO_2 and MnO_2 are formed when the calcination temperature is 400 °C. Both oxides can promote the formation of nitrate and nitrite, and then react with adsorbed NH_3 to generate NH_4NO_2 and NH_4NO_3, which can finally decompose into N_2 and H_2O (L–H mechanism).[37,48] When one of the H atoms in NH_3 is used, the resulting intermediate NH_2 reacts with NO to form NH_2NO, decomposing to form N_2 and H_2O (E-R mechanism).[49,50] Based on the above analysis, a possible reaction mechanism of the Mn_6Zr_1 catalyst is summarized in Fig. 12. Mn_6Zr_1 had the highest desorption capacity for NH_3, and its surface had the most vital adsorption capacity for NH_3. This contributes to the dehydrogenation and activation of NH_3, promotes the process of E–R and L–H, and improves its catalytic performance.

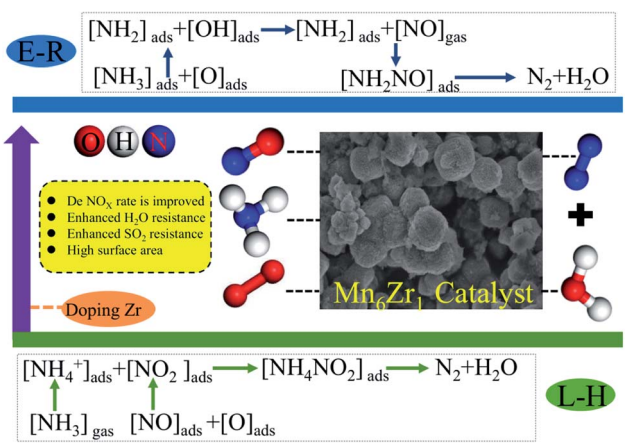

Fig. 12 NH_3-SCR reaction mechanism of the Mn_6Zr_1 catalyst.

4. Conclusions

In this work, Mn_xZr_1 series catalysts were prepared by a coprecipitation method, and the influence of zirconium-doped MnO_x catalysts on their SCR activity was studied. The results show that the Mn_6Zr_1 catalyst had the best catalytic activity when the molar ratio of Mn/Zr was 6 : 1, and the calcination temperature was 400 °C. Under the condition of 125–250 °C, the NO_x conversion rate could reach more than 90%, and the optimal conversion efficiency could reach 97%. Its resistance to SO_2 and H_2O was measured at optimum temperature, and it showed good resistance to sulfur and water. Meanwhile, the doping of zirconium into the MnO_x catalyst enhanced its physical properties, such as increasing the specific surface area, pore size, and pore volume of the catalyst. Moreover, the contents of MnO_2 species and O_α on the catalyst surface increased. The results of NH_3-TPD and H_2-TPR showed that zirconium doping also changed the acid properties of the catalyst and enhanced the redox performance of the catalyst, which is the main reason for the excellent activity of the catalyst. In summary, zirconium was successfully doped into the MnO_x catalyst, and the catalytic performance of the catalyst was significantly improved.

Conflicts of interest

All authors declare they have no conflict of interest to disclose in the context of this study.

Acknowledgements

This work was supported by the National Natural Science Foundation of China (U1504217, 51676064, 51306046) and the Innovative Research Team of Henan Polytechnic University (T2020-3).

References

1 X. Hu, Q. Shi, H. Zhang, P. Wang, S. Zhan and Y. Li, *Catal. Today*, 2017, **297**, 17–26.
2 Y. Zhang, Y. Zheng, X. Wang and X. Lu, *Catal. Commun.*, 2015, **62**, 57–61.
3 D. W. Kwon, K. H. Park and S. C. Hong, *Chem. Eng. J.*, 2016, **284**, 315–324.
4 G. Hu, J. Yang, Y. Tian, B. Kong, Q. Liu, S. Ren, J. Li and M. Kong, *Mater. Res. Bull.*, 2018, **104**, 112–118.

5 A. Shi, X. Wang, T. Yu and M. Shen, *Appl. Catal., B*, 2011, **106**, 359–369.
6 Q. Jin, Y. Shen, C. Mei, Y. Zhang and Y. Zeng, *Catal. Today*, 2020, **5**, 1–11.
7 H. Jiang, C. Wang, H. Wang and M. Zhang, *Mater. Lett.*, 2016, **168**, 17–19.
8 M. Casapu, O. Kröcher and M. Elsener, *Appl. Catal., B*, 2009, **88**, 413–419.
9 F. Gao, X. Tang, H. Yi, S. Zhao, J. Wang, Y. Shi and X. Meng, *Appl. Surf. Sci.*, 2018, **443**, 103–113.
10 X. Wang, S. Wu, W. Zou, S. Yu, K. Gui and L. Dong, *Chin. J. Catal.*, 2016, **37**, 1314–1323.
11 S. Gao, X. Chen, H. Wang, J. Mo, Z. Wu, Y. Liu and X. Weng, *J. Colloid Interface Sci.*, 2013, **394**, 515–521.
12 M. Kantcheva, I. Cayirtepe, A. Naydenov and G. Ivanov, *Catal. Today*, 2011, **176**, 437–440.
13 S. Chen, Q. Yan, C. Zhang and Q. Wang, *Catal. Today*, 2019, **327**, 81–89.
14 N. Fang, J. Guo, S. Shu, H. Luo, J. Li and Y. Chu, *J. Taiwan Inst. Chem. Eng.*, 2018, **93**, 277–288.
15 J. Ji, M. Jing, X. Wang, W. Tan, K. Guo, L. Li, X. Wang, W. Song, L. Cheng, J. Sun, W. Song, C. Tang, J. Liu and L. Dong, *J. Catal.*, 2021, **399**, 212–223.
16 H. Jiang, B. Guan, X. Peng, R. Zhan, H. Lin and Z. Huang, *Chem. Eng. J.*, 2020, **379**, 1–15.
17 F. Gao, E. D. Walter, M. Kollar, Y. Wang, J. Szanyi and C. H. F. Peden, *J. Catal.*, 2014, **319**, 1–14.
18 L. Ma, C. Y. Seo, M. Nahata, X. Chen, J. Li and J. W. Schwank, *Appl. Catal., B*, 2018, **232**, 246–259.
19 X. Wu, Y. Feng, X. Liu, L. Liu, Y. Du and Z. Li, *Appl. Surf. Sci.*, 2019, **495**, 1–13.
20 X. Tang, C. Wang, F. Gao, Y. Ma, H. Yi, S. Zhao and Y. Zhou, *J. Environ. Chem. Eng.*, 2020, **8**, 1–10.
21 B. Jia, J. Guo, H. Luo, S. Shu, N. Fang and J. Li, *Appl. Catal., A*, 2018, **553**, 82–90.
22 P. Gong, J. Xie, D. Fang, F. He, F. Li and K. Qi, *Appl. Surf. Sci.*, 2020, **505**, 1–9.
23 X. Tang, J. Hao, W. Xu and J. Li, *Catal. Commun.*, 2007, **8**, 329–334.
24 Q. H. Yan, S. N. Chen, L. Qiu, Y. S. Gao, D. O'Hare and Q. Wang, *Dalton Trans.*, 2018, **47**, 2992–3004.
25 H. Li, G. Zhu, Z. Yang, Z. Wang and Z. H. Liu, *J. Colloid Interface Sci.*, 2010, **345**, 228–233.
26 C. Yang, L. Liao, G. Lv, L. Wu, L. Mei and Z. Li, *J. Colloid Interface Sci.*, 2016, **479**, 115–120.
27 P. Zhang, G. R. Qian, H. F. Cheng, J. Yang, H. S. Shi and R. L. Frost, *Spectrochim Acta A*, 2011, **79**, 548–553.
28 Y. S. Shen, Y. F. Ma and S. M. Zhu, *Catal. Sci. Technol.*, 2012, **2**, 589–599.
29 Q. Liu, J. J. Gao, F. N. Gu, X. P. Lu, Y. J. Liu, H. F. Li, Z. Y. Zhong, B. Liu, G. W. Xu and F. B. Su, *J. Catal.*, 2015, **326**, 127–138.
30 N. J. Fang, J. X. Guo, S. Shu, H. D. Luo, Y. H. Chu and J. J. Li, *Chem. Eng. J.*, 2017, **325**, 114–123.
31 X. Y. Du, C. T. Li, L. K. Zhao, J. Zhang, L. Gao, J. J. Sheng, Y. Y. Yi, J. Q. Chen and G. M. Zeng, *Appl. Catal., B*, 2018, **232**, 37–48.
32 B. X. Shen, F. M. Wang and T. Liu, *Powder Technol.*, 2014, **253**, 152–157.
33 R. Wang, Z. Hao, Y. Li, G. Liu, H. Zhang, H. Wang, Y. Xia and S. Zhan, *Appl. Catal., B*, 2019, **258**, 1–9.
34 S. Chen, M. A. Vasiliades, Q. Yan, G. Yang, X. Du, C. Zhang, Y. Li, T. Zhu, Q. Wang and A. M. Efstathiou, *Appl. Catal., B*, 2020, **277**, 1–19.
35 J. Liu, X. Li, Q. Zhao, J. Ke, H. Xiao, X. Lv, S. Liu, M. Tadé and S. Wang, *Appl. Catal., B*, 2017, **200**, 297–308.
36 H. Xu, Y. Wang, Y. Cao, Z. Fang, T. Lin, M. Gong and Y. Chen, *Chem. Eng. J.*, 2014, **240**, 62–73.
37 J. Li, J. Guo, X. Shi, X. Wen, Y. Chu and S. Yuan, *Appl. Surf. Sci.*, 2020, **534**, 1–13.
38 Z. Yan, J. Yang, X. Ge, J. Yu, L. Wei, T. Yang, B. He, X. Wang and L. Liu, *Appl. Surf. Sci.*, 2019, **491**, 579–589.
39 T. Zhang, J. Liu, D. Wang, Z. Zhao, Y. Wei, K. Cheng, G. Jiang and A. Duan, *Appl. Catal., B*, 2014, **148–149**, 520–531.
40 P. Wang, D. Yu, L. Zhang, Y. Ren, M. Jin and L. Lei, *Appl. Catal., A*, 2020, **607**, 117806.
41 X. Wu, Y. Feng, Y. Du, X. Liu, C. Zou and Z. Li, *Appl. Surf. Sci.*, 2019, **467–468**, 802–810.
42 D. Fang, J. Xie, H. Hu, H. Yang, F. He and Z. Fu, *Chem. Eng. J.*, 2015, **271**, 23–30.
43 Q. Yan, S. Chen, C. Zhang, Q. Wang and B. Louis, *Appl. Catal., B*, 2018, **238**, 236–247.
44 E. Gao, G. Sun, W. Zhang, M. T. Bernards, Y. He, H. Pan and Y. Shi, *Chem. Eng. J.*, 2020, **380**, 1–12.
45 J. Gao, Y. Han, J. Mu, S. Wu, F. Tan, Y. Shi and X. Li, *J. Colloid Interface Sci.*, 2018, **516**, 254–262.
46 X. Wu, H. Meng, Y. Du, J. Liu, B. Hou and X. Xie, *J. Catal.*, 2020, **384**, 72–87.
47 B. Jia, J. Guo, S. Shu, N. Fang, J. Li and Y. Chu, *Mol. Catal.*, 2017, **443**, 25–37.
48 S. Xie, L. Li, L. Jin, Y. Wu, H. Liu, Q. Qin, X. Wei, J. Liu, L. Dong and B. Li, *Appl. Surf. Sci.*, 2020, **515**, 1–12.
49 F. Gao, C. Yang, X. Tang, H. Yi and C. Wang, *J. Environ. Sci.*, 2022, **113**, 204–218.
50 M. Guo, Q. Liu, C. Liu, X. Wang, Y. Bi, B. Fan, D. Ma, X. Liang and Z. Li, *Chem. Eng. J.*, 2021, **413**, 1–10.